Journal of Computational and Applied Mathematics 246 (2013) 185–194

Contents lists available at SciVerse ScienceDirect

Journal of Computational and Applied Mathematics

journal homepage: www.elsevier.com/locate/cam

# Subspace analysis to alleviate the volumetric locking in the 3D solid-shell EFG method☆

Ana Graça [a,*], Rui P.R. Cardoso [a], Jeong Whan Yoon [b,a]

[a] Center for Mechanical Technology and Automation (TEMA) — University of Aveiro, Campus Univ. de Santiago, 3810-193 Aveiro, Portugal

[b] Australian Advanced Manufacturing Research Centre, Faculty of Engineering & Industrial Sciences, Swinburne University of Technology, Hawthorn, Victoria, 3122, Australia

ARTICLE INFO

*Article history:*
Received 31 January 2012
Received in revised form 11 September 2012

*Keywords:*
Meshless methods
EFG
B-bar
EAS
Subspace analysis

ABSTRACT

The main objective of this work is to reduce the volumetric locking pathology at the Element Free Galerkin (EFG) 3D solid-shell meshless method. For this purpose, a subspace analysis is performed in order to extract the linearly independent incompressible deformation modes that can be reproduced by different background integration cells. Additional deformation modes reproduced by a cell configuration produces more flexibility for the meshless formulation. The Enhanced Assumed Strain (EAS) method is blended with the EFG formulation in such a way that additional (mathematical) variables are included in the formulation increasing its flexibility for nearly incompressible materials. Three numerical examples show the effect of the EAS formulation in alleviating the locking pathology for an almost incompressible material condition.



## 1. Introduction

The development of 3D solid-shell elements for the Finite Element Method (FEM) increased considerably during the past years partially because of the modelling of shell-type structures without rotational degrees of freedom (see for example [1]). It is well known that solid-shell elements have some locking pathologies that, if not properly treated, can lead to erroneous results. The most typical locking problems are the ones related to incompressibility, Poisson's locking and also the transverse shear locking. Many methods to solve these locking issues were already proposed in the last several years, but they were mainly oriented for the FEM analysis.

Recently, Recio et al. [2], implemented the Enhanced Assumed Strain (EAS) method for the plane strain Element Free Galerkin (EFG) method and compared the results with the B-Bar approach. The main objective of their work was to alleviate the volumetric locking.

The subspace analysis was introduced successfully in [3] for plane strain quadrilateral elements. This work verified that some isochoric deformation modes reproduced by the reduced integrated element could not be reproduced accurately by a full quadrature scheme. These modes were then identified and added to the subspace of a fully integrated element by adding extra enhancing variables.

The goal of the present work is to understand and alleviate the volumetric locking for an EFG method by using a subspace analysis. The missing deformation modes will be identified similarly as it was done in [3] for the FEM plane strain quadrilateral elements and added to the basis of the EFG background cell by using the EAS method. The 3D solid-shell EFG concept is compared with the classical EFG, the B-Bar approach and the EAS method in terms of accuracy.

☆ This work has been funded by Fundação para a Ciência e Tecnologia (FCT), under Ph.D. grant SFRH/BD/71483/2010. The financial support from Ministério da Ciência e Ensino Superior (FCT-Portugal) under PTDC/EME-TME/105237/2008 is gratefully acknowledged.

* Corresponding author.
*E-mail address:* ana.graca@ua.pt (A. Graça).

0377-0427/$ – see front matter © 2012 Elsevier B.V. All rights reserved.
doi:10.1016/j.cam.2012.09.013

## 2. Element Free Galerkin

The Moving Least Squares (MLS) approximation was described in [4] and it is used in the EFG method to estimate the function $u(\mathbf{x})$, as shown below:

$$u(\mathbf{x}) \approx u^h(\mathbf{x}) = \sum_j^m p_j(\mathbf{x}) a_j(\mathbf{x}) \equiv \mathbf{p}^{\mathrm{T}}(\mathbf{x})\mathbf{a}(\mathbf{x}), \tag{1}$$

where $\mathbf{a}(\mathbf{x})$ represents the unknown parameters, $\mathbf{p}^{\mathrm{T}}(\mathbf{x})$ and $m$ are the polynomial and its order, respectively. In this paper, a linear basis polynomial will be considered as follows:

$$\mathbf{p}^{\mathrm{T}}(\mathbf{x}) = [1, x, y, z], \quad m = 4, \tag{2}$$

meaning that, at least four neighbours are considered in the domain of influence of each point for obtaining the unknown parameters $\mathbf{a}(\mathbf{x})$. The approximation for the displacement field becomes

$$\mathbf{u}^h(\mathbf{x}) = \sum_{I=1}^n \Phi_I(\mathbf{x})\mathbf{u}_I \tag{3}$$

where the approximation functions $\Phi_I(\mathbf{x})$ are given by

$$\Phi_I(\mathbf{x}) = \sum_{j=0}^m p_j(\mathbf{x}) \left(\mathbf{A}^{-1}(\mathbf{x})\mathbf{B}(\mathbf{x})\right)_{jI} \tag{4}$$

with

$$\mathbf{A} = \sum_{I=1}^n w(\mathbf{x} - \mathbf{x}_I)\mathbf{p}^{\mathrm{T}}(\mathbf{x}_I)\mathbf{p}(\mathbf{x}_I) \tag{5}$$

$$\mathbf{B}(\mathbf{x}) = [w(\mathbf{x} - \mathbf{x}_1)\mathbf{p}(\mathbf{x}_1), w(\mathbf{x} - \mathbf{x}_2)\mathbf{p}(\mathbf{x}_2), \ldots, w(\mathbf{x} - \mathbf{x}_n)\mathbf{p}(\mathbf{x}_n)] \tag{6}$$

and $w(\mathbf{x} - \mathbf{x}_I)$ is the weight function. The EFG approximation functions do not satisfy the Kronecker delta property: $\Phi_I(x_J) \neq \delta_{IJ}$ and therefore the imposition of essential boundary conditions is not as straightforward as in the finite element method. For this reason, a constraint method is applied in such a way that essential boundary conditions can be fulfilled. In this work, Lagrange multipliers were used to impose the local constraints for boundary conditions.

According to [5], the discrete equations of the Galerkin Formulation can be described as follows:

$$\begin{bmatrix} \mathbf{K} & \mathbf{G} \\ \mathbf{G}^T & 0 \end{bmatrix} \begin{bmatrix} \mathbf{u} \\ \lambda \end{bmatrix} = \begin{bmatrix} \mathbf{f} \\ \mathbf{q} \end{bmatrix} \tag{7}$$

where

$$\mathbf{K}_{IJ} = \int_\Omega \mathbf{B}_I^T \mathbf{D}\mathbf{B}_J d\Omega; \quad \mathbf{B}_I = \begin{bmatrix} \Phi_{I,x} & 0 & 0 \\ 0 & \Phi_{I,y} & 0 \\ 0 & 0 & \Phi_{I,z} \\ 0 & \Phi_{I,z} & \Phi_{I,y} \\ \Phi_{I,z} & 0 & \Phi_{I,x} \\ \Phi_{I,y} & \Phi_{I,x} & 0 \end{bmatrix} \tag{8}$$

$$\mathbf{G}_{IK} = -\int_{\Gamma_u} \Phi_I \mathrm{N}_K d\Gamma; \qquad \mathbf{f}_I = \int_{\Gamma_t} \Phi_I \bar{\mathbf{t}} d\Gamma + \int_\Omega \Phi_I \mathbf{b} d\Omega; \qquad \mathbf{q}_K = -\int_{\Gamma_u} \mathrm{N}_K \bar{\mathbf{u}} d\Gamma \tag{9}$$

in which $\mathrm{N}_K$ is a Lagrange multiplier interpolation function, $\mathbf{u}$ is a vector with the nodal displacements, $\lambda$ represents the Lagrange multipliers and $\mathbf{D}$ is the constitutive matrix for the plane strain condition.

## 3. B-Bar method

When large domains of influence are considered to obtain the EFG approximation functions, locking problems are alleviated leading to an approximation almost free of locking pathologies [6]. However, choosing large domains of influence increases computational cost, too. Thus, mixed formulations were introduced in the EFG method as an alternative remedy to alleviate the volumetric locking. In the EFG method, a background mesh with Gauss integration points is still required to integrate the stiffness matrix [7]. This EFG characteristic allows the use of FEM tools to improve the EFG method. One of these tools is the B-Bar formulation that was first developed for the classical FEM in [8] and later adapted to EFG in [2]. In the B-Bar approach, the $\mathbf{B}_I$ matrix in Eq. (8) is separated into two different components: dilatational, $\mathbf{B}_I^{\mathrm{dil}}$, and deviatoric, $\mathbf{B}_I^{\mathrm{dev}}$, so that $\mathbf{B}_I^{\mathrm{dev}} = \mathbf{B}_I - \mathbf{B}_I^{\mathrm{dil}}$. To achieve an effective formulation for nearly incompressible materials, the dilatational component is

improved by integrating it with a reduced integration rule. This term is designated by $\bar{\mathbf{B}}_I^{\text{dil}}$ and has the following format

$$\bar{\mathbf{B}}_I^{\text{dil}} = \frac{1}{3}\begin{bmatrix} \bar{\Phi}_{I,x} & \bar{\Phi}_{I,y} & \bar{\Phi}_{I,z} \\ \bar{\Phi}_{I,x} & \bar{\Phi}_{I,y} & \bar{\Phi}_{I,z} \\ \bar{\Phi}_{I,x} & \bar{\Phi}_{I,y} & \bar{\Phi}_{I,z} \\ 0 & 0 & 0 \\ 0 & 0 & 0 \\ 0 & 0 & 0 \end{bmatrix} \tag{10}$$

in which the EFG approximation functions are constructed for the reduced integration rule. Therefore,

$$\bar{\mathbf{B}}_I = \mathbf{B}_I^{\text{dev}} + \bar{\mathbf{B}}_I^{\text{dil}}. \tag{11}$$

Replacing $\mathbf{B}_I$ by $\bar{\mathbf{B}}_I$ in Eq. (8) leads to

$$K_{IJ} = \int_{\Omega} \left[\mathbf{B}_I^{\text{dev}} + \bar{\mathbf{B}}_I^{\text{dil}}\right]^{\mathrm{T}} \mathbf{D} \left[\mathbf{B}_J^{\text{dev}} + \bar{\mathbf{B}}_J^{\text{dil}}\right] d\Omega. \tag{12}$$

In this work it will be considered two configurations for the background cells: (1) for a 8-nodes background cell (4 nodes in the bottom and 4 nodes in the top surfaces) a full integration of $2 \times 2 \times 2$ Gauss points and a reduced integration of $1 \times 1 \times 1$ Gauss points will be considered; (2) for a 18-nodes (9 nodes in the bottom and 9 nodes in the top surfaces) a full integration $3 \times 3 \times 2$ and a reduced integration of $2 \times 2 \times 1$ Gauss points in a middle plane through the thickness direction will be considered.

## 4. Enhanced Assumed Strain method

The Enhanced Assumed Strain (EAS) method can be explained as a variational principle where the strain field is composed of a sum of two independent strain components:

$$\boldsymbol{\epsilon} = \partial \mathbf{u} + \boldsymbol{\epsilon}^{\alpha}, \tag{13}$$

where $\boldsymbol{\epsilon}^{\alpha}$ is an enhanced strain field independent of the displacement gradient $\partial \mathbf{u}$.

The Veubeke–Hu–Washizu [9] three-field variational principle, in which displacements, strains and stresses are treated as independent variables, can be stated as

$$\delta\left(\int_{\Omega} w\left(\boldsymbol{\epsilon}\right) d\Omega - \int_{\Omega} \mathbf{f} \cdot \mathbf{u}\, d\Omega - \int_{\Gamma} \mathbf{T} \cdot \mathbf{u}\, d\Gamma - \int_{\Omega} \boldsymbol{\sigma} : \boldsymbol{\epsilon}^{\alpha}\, d\Omega\right) = 0, \tag{14}$$

where $w\left(\boldsymbol{\epsilon}\right)$ is the strain energy density, $\mathbf{f}$ represents the volume forces at the domain $\Omega$ of the body and $\mathbf{T}$ is the stress vector at the body's boundary $\Gamma$.

From [10] formulation, the stress field $\boldsymbol{\sigma}$ is assumed to be orthogonal to the enhanced strain field $\boldsymbol{\epsilon}^{\alpha}$, that is

$$\int_{\Omega} \boldsymbol{\sigma} : \boldsymbol{\epsilon}^{\alpha}\, d\Omega = 0. \tag{15}$$

Several EAS methods have been implemented successfully within the scope of finite elements. For instance, the works of Simo and co-workers [11], Reese and Wriggers [12], César de Sá and Natal Jorge [3], and Cardoso et al. [1] are the examples of EAS methods in the finite element technology.

Blending an EAS method with an EFG method is equivalent to considering an additional enhancing deformation field as shown in Eq. (13). This can be translated by the product of an enhancing strain–displacement matrix with the enhancing extra variables $\boldsymbol{\alpha}$ as follows:

$$\boldsymbol{\epsilon} = \partial \mathbf{u} + \boldsymbol{\epsilon}^{\alpha} = \mathbf{B}_I^{\partial u} \cdot \mathbf{u}_I + \mathbf{B}_K^{\alpha} \cdot \boldsymbol{\alpha}_K \tag{16}$$

where

$$\mathbf{B}_K^{\alpha} = \frac{|\mathbf{J}_0|}{|\mathbf{J}|} \mathbf{T}_0 \mathbf{M}_{\alpha} \tag{17}$$

and the Jacobian matrix $\mathbf{J}$ that relates the global and natural coordinate system is given by the following matrix:

$$\mathbf{J} = \begin{bmatrix} \dfrac{\partial x_1}{\partial \xi} & \dfrac{\partial x_2}{\partial \xi} & \dfrac{\partial x_3}{\partial \xi} \\ \dfrac{\partial x_1}{\partial \eta} & \dfrac{\partial x_2}{\partial \eta} & \dfrac{\partial x_3}{\partial \eta} \\ \dfrac{\partial x_1}{\partial \zeta} & \dfrac{\partial x_2}{\partial \zeta} & \dfrac{\partial x_3}{\partial \zeta} \end{bmatrix}. \tag{18}$$

$|\mathbf{J}|$ and $|\mathbf{J}_0|$ are the Jacobian's determinant for full and reduced integration methods, respectively. $\mathbf{M}_{\alpha}$ is the enhancing strain–displacement matrix in the natural coordinate system. The dimensions of this matrix depend on the number of enhancing variables $\boldsymbol{\alpha}$, which are closely related with the subspace analysis performed in the next section. $\mathbf{T}_0$ is a second-order transformation tensor.

For the construction of the EAS strain–displacement field $\mathbf{M}_\alpha$ in Eq. (17), it is used a bubble shape function, $N_\alpha$, defined at the cell's centre as follows:

$$N_\alpha = (1-\xi^2)(1-\eta^2)(1-\zeta^2). \tag{19}$$

As can be seen from the subspace analysis of the next section, it will be used 9 additional enhancing variables $\boldsymbol{\alpha}$. Thus, the enhancing strain–displacement matrix $\mathbf{M}_9$ becomes

$$\mathbf{M}_9 = \begin{bmatrix} \frac{\partial N_\alpha}{\partial \xi} & 0 & 0 & \frac{\partial^2 N_\alpha}{\partial \xi^2} & 0 & 0 & \frac{\partial N_\alpha^2}{\partial \xi \partial \eta} & \frac{\partial N_\alpha^2}{\partial \xi \partial \zeta} & \frac{\partial N_\alpha^2}{\partial \eta \partial \zeta} \\ 0 & \frac{\partial N_\alpha}{\partial \eta} & 0 & 0 & \frac{\partial^2 N_\alpha}{\partial \eta^2} & 0 & \frac{\partial N_\alpha^2}{\partial \xi \partial \eta} & \frac{\partial N_\alpha^2}{\partial \xi \partial \zeta} & \frac{\partial N_\alpha^2}{\partial \eta \partial \zeta} \\ 0 & 0 & \frac{\partial N_\alpha}{\partial \zeta} & 0 & 0 & \frac{\partial^2 N_\alpha}{\partial \zeta^2} & \frac{\partial N_\alpha^2}{\partial \xi \partial \eta} & \frac{\partial N_\alpha^2}{\partial \xi \partial \zeta} & \frac{\partial N_\alpha^2}{\partial \eta \partial \zeta} \\ 0 & 0 & 0 & \frac{\partial N_\alpha}{\partial \eta} & \frac{\partial N_\alpha}{\partial \xi} & 0 & 0 & 0 & 0 \\ 0 & 0 & 0 & \frac{\partial N_\alpha}{\partial \zeta} & 0 & \frac{\partial N_\alpha}{\partial \xi} & 0 & 0 & 0 \\ 0 & 0 & 0 & 0 & \frac{\partial N_\alpha}{\partial \zeta} & \frac{\partial N_\alpha}{\partial \eta} & 0 & 0 & 0 \end{bmatrix}. \tag{20}$$

From the variational principle in Eqs. (14)–(15), the final set of equilibrium equations becomes

$$\begin{bmatrix} \mathbf{K}_{uu} & \mathbf{K}_{u\alpha} \\ \mathbf{K}_{\alpha u} & \mathbf{K}_{\alpha\alpha} \end{bmatrix} \begin{bmatrix} \mathbf{u} \\ \boldsymbol{\alpha} \end{bmatrix} = \begin{bmatrix} \mathbf{f} \\ 0 \end{bmatrix} \tag{21}$$

where

$$\mathbf{K}_{uu} = \int_\Omega \left(\mathbf{B}^{\partial u}\right)^T \mathbf{D}\,\mathbf{B}^{\partial u}\, d\Omega; \qquad \mathbf{K}_{u\alpha} = \int_\Omega \left(\mathbf{B}^{\partial u}\right)^T \mathbf{D}\,\mathbf{B}^{\alpha}\, d\Omega; \qquad \mathbf{K}_{\alpha\alpha} = \int_\Omega (\mathbf{B}^{\alpha})^T\, \mathbf{D}\,\mathbf{B}^{\alpha}\, d\Omega. \tag{22}$$

For the EAS method in this work, the additional enhancing variables can be condensed at an element or background cell level, giving rise to a new condensed stiffness matrix, $\mathbf{K}_{\text{cond}}$, that can be introduced directly in the original set of equations (7)

$$\mathbf{K}_{\text{cond}} = \mathbf{K}_{uu} - \mathbf{K}_{u\alpha}\mathbf{K}_{\alpha\alpha}^{-1}\mathbf{K}_{\alpha u}. \tag{23}$$

The possibility to eliminate the enhancing variables at the cell's level is a positive aspect as far as it does not deteriorate considerably the computational performance of the meshless formulation and does not increase the bandwidth of the global system of equations.

### 4.1. Subspace analysis

For small incompressible deformations the following incompressibility condition must be satisfied

$$\int_\Omega \text{div}\,(\mathbf{u})\; d\Omega = 0. \tag{24}$$

The overall incompressibility condition of Eq. (24) can be regarded as a local constraint to the variational principle from Eq. (14) where it can be inserted in the variational via for example, Lagrange multipliers. When discretized in the context of a EFG formulation, the incompressibility condition should be satisfied at least at the Gauss integration points. The discretized incompressibility condition can thus be written as [3]

$$(\mathbf{m}^{\mathrm{T}} \cdot \mathbf{B}_i) \cdot \mathbf{u} = 0, \tag{25}$$

where $i$ stands for the Gauss point number and $\mathbf{m}^{\mathrm{T}} = \begin{bmatrix} 1 & 1 & 1 & 0 & 0 & 0 \end{bmatrix}$.

The $\mathbf{null}(\mathbf{m}^{\mathrm{T}} \cdot \mathbf{B}_i)$ provides the different linearly independent deformation modes reproduced by the background cell that fulfil the incompressibility condition at Eq. (25). These modes define the subspace of admissible incompressible deformations.

The incompressible deformation modes will be shown in this work for two background cell's configurations (regarding the integration rule): (1) full integration ($3 \times 3 \times 2$), originating 36 linearly independent incompressible modes; (2) reduced integration ($2 \times 2 \times 1$), giving rise to 10 additional incompressible deformation modes. More incompressible deformation modes means more flexibility for the cell's configuration alleviating the locking pathology. However, the reduced integrated cell brings instability or hourglass deformation patterns. The main goal is to include those 10 additional deformation modes at the full integrated cell configuration. This can be achieved with the Enhanced Assumed Strain Method explained in the previous section.

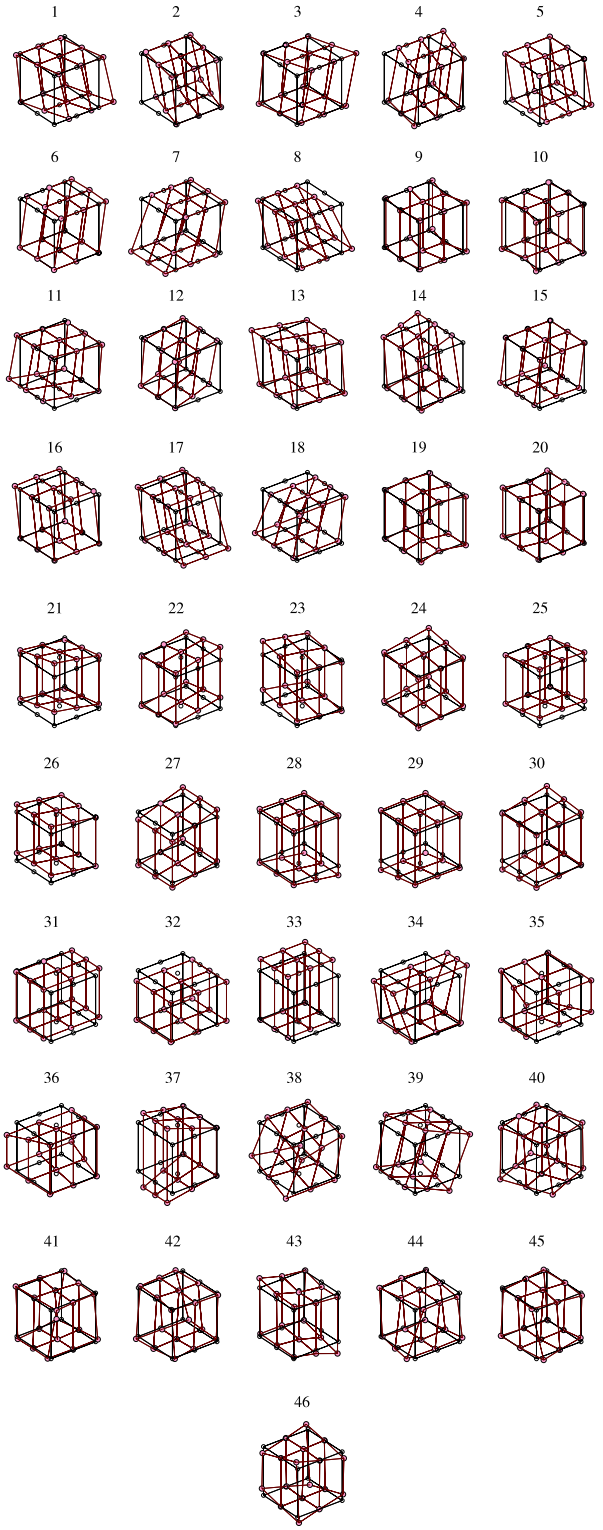


**Fig. 1.** Linearly independent incompressible modes.

In Fig. 1 are represented the 46 linearly independent incompressible modes that can be obtained from the reduced integration rule. The first 10 modes are related to the displacement along the $x$-axis and include edges translations as well as hourglass deformation patterns. The modes between numbers 11–20 and 21–30 are related to displacements along the $y$-axis and $z$-axis, respectively. The modes between numbers 31–37 represent the expansion and contraction of the cell,

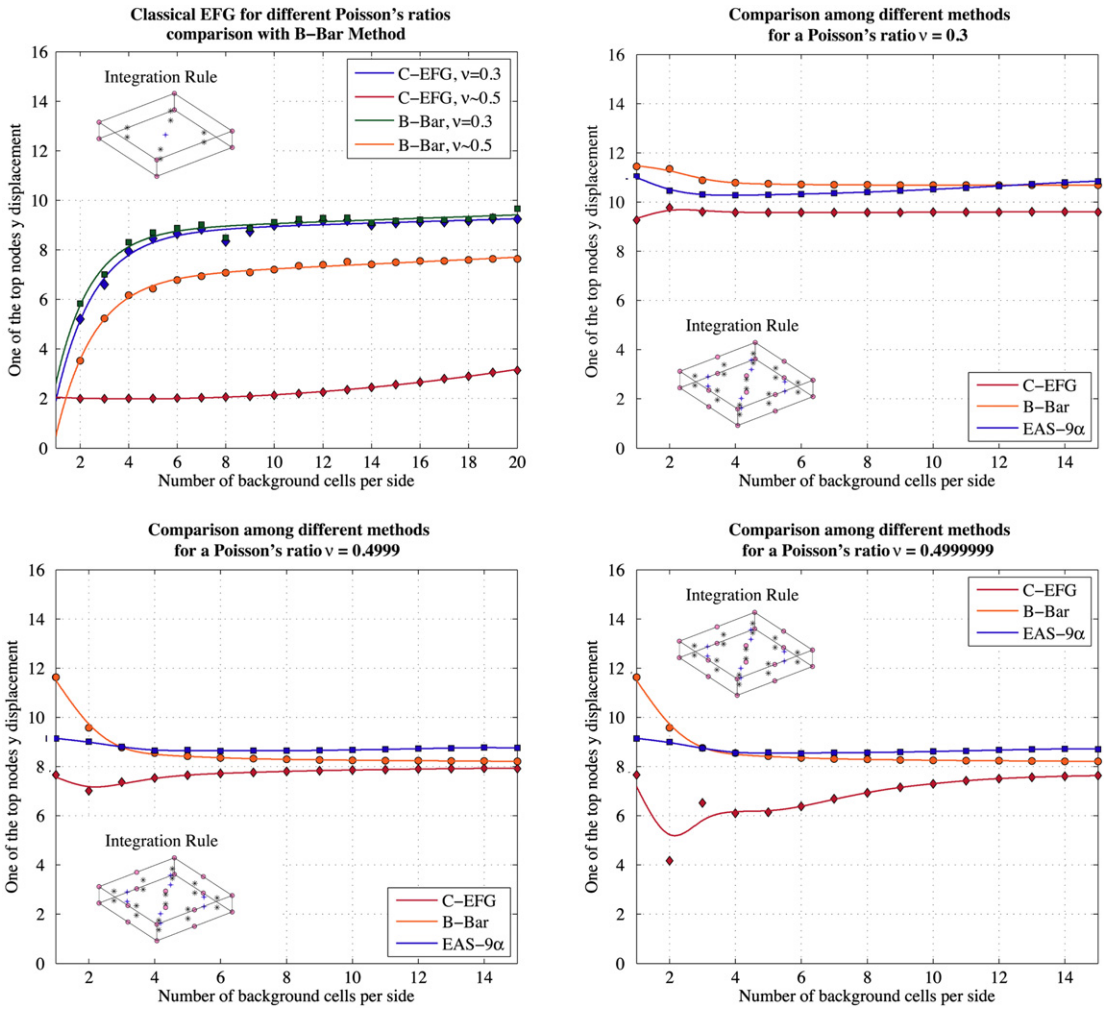


**Fig. 2.** Convergence results for the trapezoidal body problem.

modes 38–40 are considered the rotational modes while modes 41–46 can be considered non-physical modes. Because the EFG method is not interpolatory, the perception of the deformation modes at Fig. 1 can be hard to identify. Also, although the deformation modes are linearly independent, they can appear mixed together and a pure distinction between translational, rotational, expansion and contraction modes is difficult to be obtained.

## 5. Numerical examples

### *5.1. Trapezoidal body under the plane strain condition*

This example is a plane strain version of Cook's membrane as described in [13]. A trapezoidal body clamped on one end and subjected to a distributed in-plane bending load, as shown in Fig. 3, is analysed. The material properties considered are: Young's modulus, $E = 240.565$ and Poisson's ratios $\nu = 0.3$, $\nu = 0.4999$ and $\nu = 0.4999999$. The loading condition is $F = 100$ and thickness, $a = 1$. Displacements along the $z$-axis are constrained in order to induce the plane strain condition.

In the first plot of Fig. 2, comparison between classical EFG and B-Bar methods reveals the locking pathology in the classical EFG method when Poisson's ratio approaches 0.5. Here, a background mesh with 8-nodes cell ($\bullet$), a full integration of $2 \times 2 \times 2$ ($*$) and a reduced integration of $1 \times 1 \times 1$ ($+$) Gauss points is used to obtain the converged solution for the $y$-displacement for one of the top nodes ($x = 48$, $y = 60$, $z = 0$).

In the other plots in Fig. 2, a $3 \times 3 \times 2$ integration rule is used for 18-nodes background cell. In this case, it is shown the importance of the enhancing formulation in improving the convergence behaviour of this cell's configuration. This fact can be easily understood because the subspace analysis showed that in order to capture the same performance of the reduced integrated cell, 10 additional incompressible deformation modes should be included. With the 9 additional enhancing variables ($\mathbf{M}_9$ EAS formulation), there were included 9 additional incompressible deformation modes, giving great flexibility to the EFG cell.

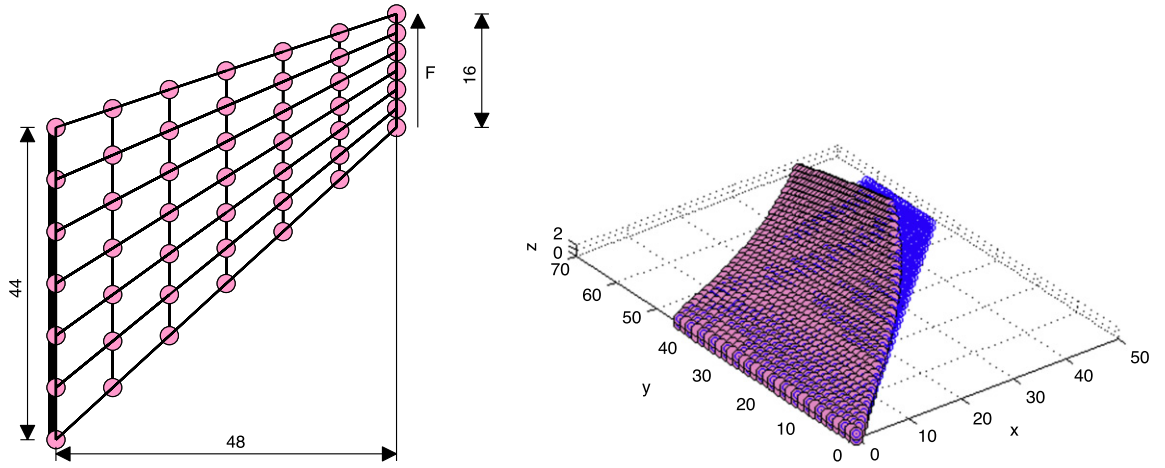


(a) Initial geometry.

(b) Deformed geometry for EAS-9$\alpha$, $\nu \approx 0.5$ and a $3 \times 3 \times 2$ integration rule.

**Fig. 3.** Trapezoidal body under plane strain condition.

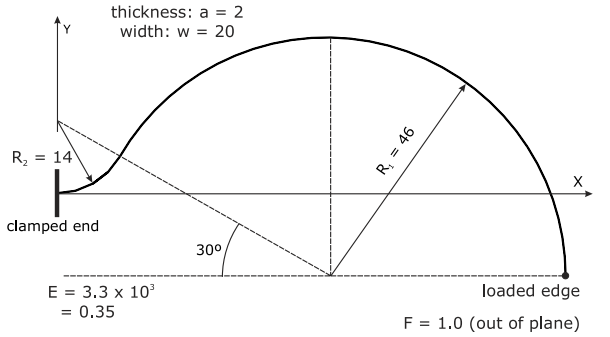


(a) Initial geometry.

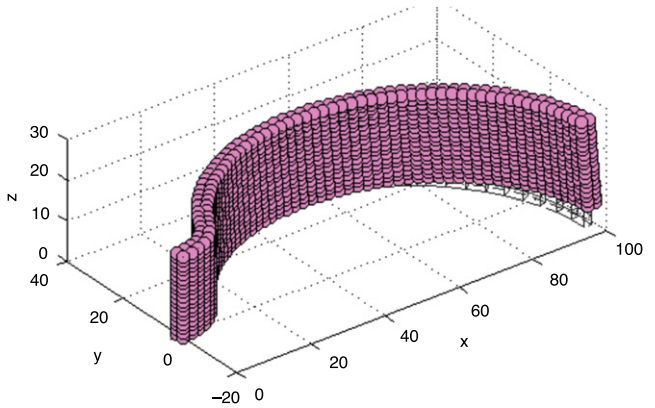


(b) Deformed geometry for EAS-9$\alpha$, $\nu \approx 0.5$ and a $3 \times 3 \times 2$ integration rule.

**Fig. 4.** Raasch's hook.

### 5.2. The Raasch's hook

Ingo Raasch, at BMW AG, presented his hook challenge in 1990 [14]. Kemp et al. [15] stated that by studying this problem it is possible to evaluate the subsequent difficulties of coupling among bending, extension, and twisting deformation. A curved strip rigidly clamped at one end with a unit load distributed along the width of the free end defines the geometry of the Raasch's hook.

Fig. 4 illustrates its top view, where two circular arcs are connected at the tangent point. Geometric, material, boundary and loading conditions considered follow the works of Knight [14] and Cardoso [16].

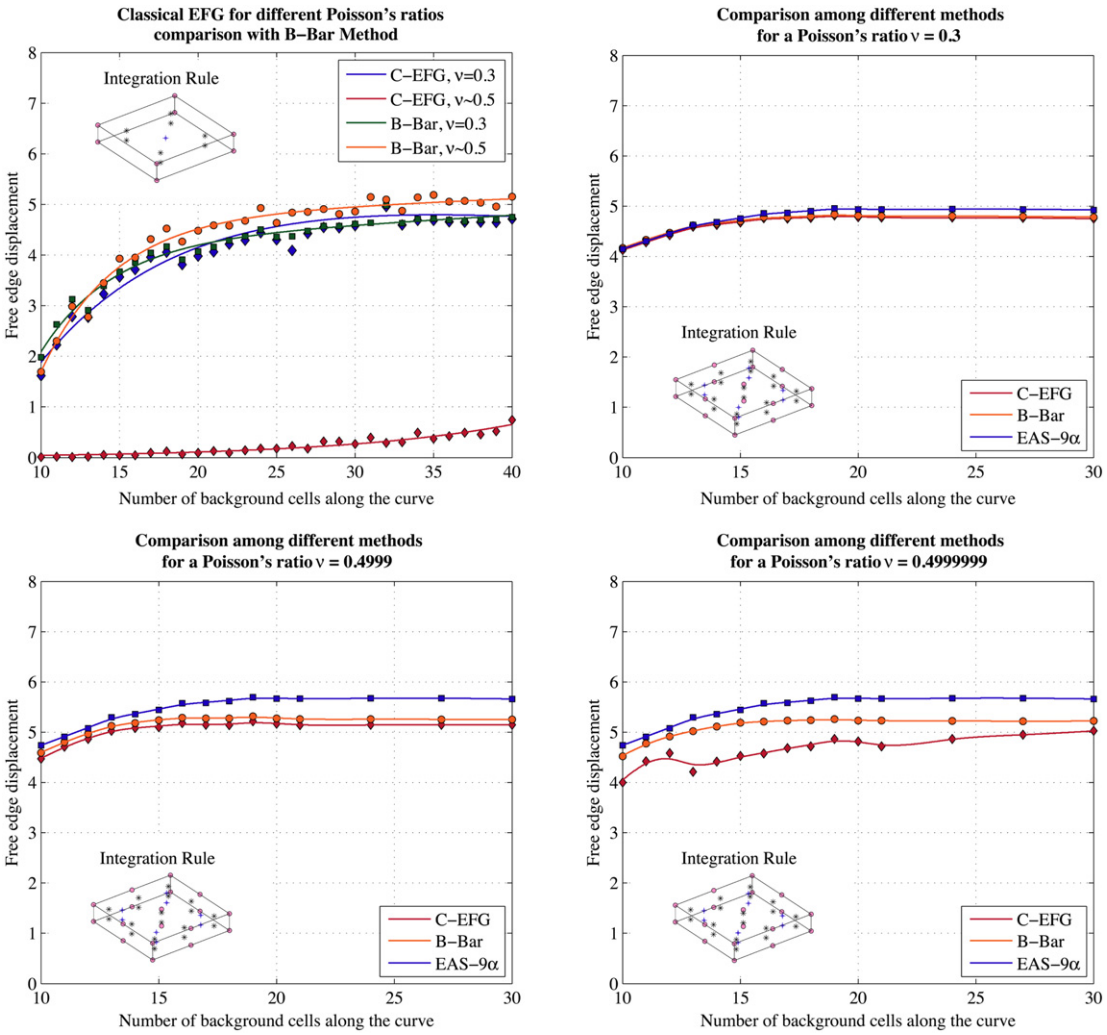


**Fig. 5.** Convergence results for Raasch's hook problem.

Fig. 5 shows convergence results for the displacement in the load direction of the free edge obtained by the same background cell topology used in the trapezoidal body example. The number of background cells along the width corresponds to the nearest minor integer of a third of the number of background cells along the curve.

As can be seen in the plots of Fig. 5, as well as in the plots of Fig. 2 for the trapezoidal body example, the classical EFG method starts having better convergence ratio for integration cells with higher order monomials for the EFG approximation functions (for cells with integration rules of $3 \times 3 \times 2$). This is because additional nodes are necessary in the domain of influence of each Gauss point, meaning that more degrees of freedom are included at each domain of influence, providing improved flexibility to the solution. However, this also means more computational time.

Another aspect worth mentioning is that the combined EFG+EAS formulation delivers more flexible behaviour even for a large value of Poisson's ratio, converging to a slightly higher tip displacement. While the B-Bar approach interpolates the dilatational field from a reduced integrated space, the EAS formulation is constructed from the subspace analysis by completely removing the dilatational deformation tensor, which may cause the slightly overestimated displacement profile.

### *5.3. Long cylinder under internal pressure*

In this example, a long cylinder under internal pressure is considered. Because of its symmetry and length, it is convenient to model a quarter of the slice assumed to be in the middle of the cylinder. The initial dimensions, geometry and boundary conditions are represented in Fig. 6. Additionally, top and bottom faces are constricted along the $z$-axis to reproduce a plane strain state. The material properties considered are: Young's modulus $E = 24000$ and Poisson's ratio $\nu = 0.3$ and $\nu \approx 0.5$. The internal pressure is $P = 100$.

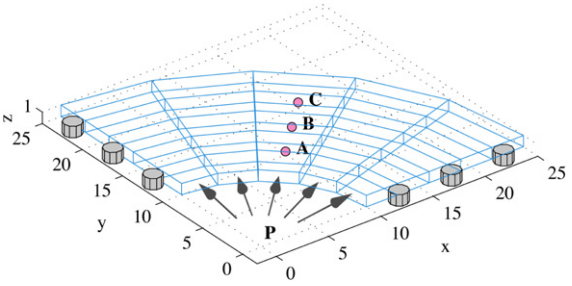


**Fig. 6.** Initial geometry and boundary conditions.

**Table 1**
Radial displacement for a Poisson's ratio $\nu \approx 0.5$.

| Method | No. nodes | Nodes | | |
|---|---|---|---|---|
| | | A | B | C |
| C-EFG | 581 | 0.0477 | 0.0362 | 0.0307 |
| | 1253 | 0.0540 | 0.0422 | 0.0347 |
| B-Bar | 581 | 0.0545 | 0.0433 | 0.0358 |
| | 1253 | 0.0557 | 0.0440 | 0.0364 |
| EAS-9$\alpha$ | 581 | 0.0600 | 0.0454 | 0.0370 |
| | 1253 | 0.0639 | 0.0463 | 0.0374 |
| Exact value | | 0.0595 | 0.0494 | 0.0434 |

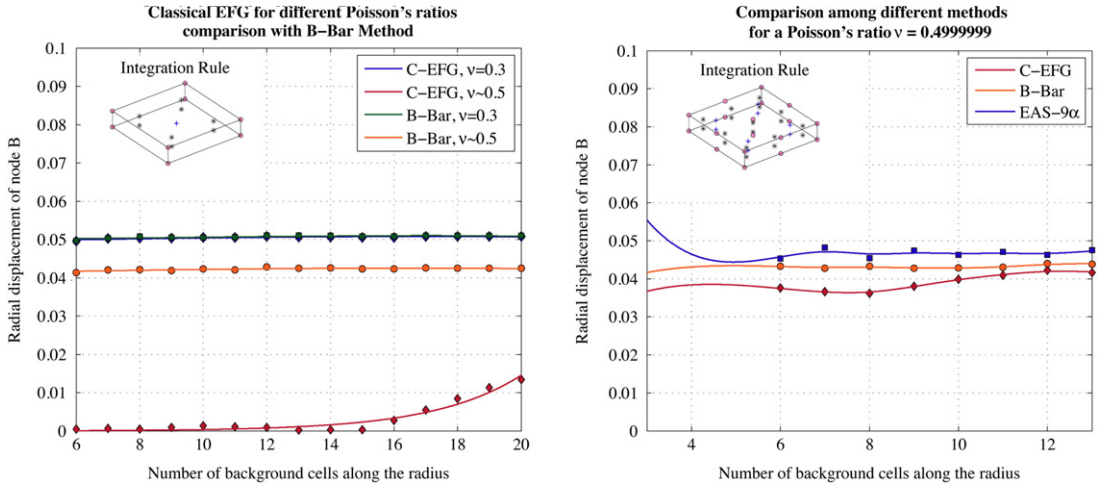


**Fig. 7.** Convergence results for a long cylinder under internal pressure.

Table 1 shows the radial displacements of the three nodes indicated in Fig. 6, obtained from the classical EFG, B-Bar and EAS-9$\alpha$ methods, for a Poisson's ratio $\nu \approx 0.5$ and considering 581 and 1253 nodes to describe the problem domain. The exact values presented derive from the analytical solution for this benchmark problem that can be found in [17]. Accordingly, the radial displacement $u_r$ is given by

$$u_r = \frac{a^2 Pr}{E\left(b^2 - a^2\right)}\left[1 - \nu + \frac{b^2}{r^2}(1+\nu)\right] \tag{26}$$

where $P$ is the internal pressure, $r$ is the radial coordinate and $a$ and $b$ are the internal and external radii of the cylinder, respectively.

In the plot on the left side of Fig. 7 an analysis for the classical EFG and B-Bar method was performed with the main objective of showing the locking of the classical EFG for an integration rule of $2 \times 2 \times 1$. The locking for the classical EFG formulation was alleviated in the plot of the right side of Fig. 7 for an integration rule of $3 \times 3 \times 2$. The explanation for this behaviour is that for a higher number of integration points more nodes are needed in the domain of influence and thus more deformation modes can be reproduced by the formulation. This can be checked also from the EAS formulation that provides more flexibility to the solution as a result of the enhancing *degrees of freedom* artificially added to the formulation.

## 6. Concluding remarks

The classical EFG method experiences the volumetric locking phenomena when a nearly incompressible material is simulated. In this paper, a subspace analysis for a 3D background meshless cell provides the capability of understanding the different incompressible deformation modes that can be reproduced for different integration rules at the cell. With the subspace analysis, it was possible to include successfully the necessary deformation patterns in the EFG formulation by means of additional enhancing variables.

The numerical results reveal that combining the EFG method with the EAS formulation has great potential in applications involving almost incompressible materials. Comparison between the proposed approach and B-Bar technique also shows that the combined EFG+EAS formulation gives more freedom or flexibility to the solution and is thus an alternative approach to the B-Bar approach for nearly incompressible materials.

## References

[1] R.P. Cardoso, J.W. Yoon, M. Mahardika, S. Choudhry, R.A. de Sousa, R.F. Valente, Enhanced assumed strain (EAS) and assumed natural strain (ANS) methods for one-point quadrature solid-shell elements, International Journal for Numerical Methods in Engineering 75 (2008) 156–187.
[2] D.P. Recio, R.M.N. Jorge, L.M.S. Dinis, Locking and hourglass phenomena in an element-free Galerkin context: the B-bar method with stabilization and an enhanced strain method, International Journal for Numerical Methods in Engineering 68 (2006) 1329–1357.
[3] J.M.A. César de Sá, R.M.N. Jorge, New enhanced strain elements for incompressible problems, International Journal for Numerical Methods in Engineering 44 (1999) 229–248.
[4] P. Lancaster, K. Salkaukas, Surfaces generated by moving least squares methods, Mathematics of Computation 37 (155) (1981) 141–158.
[5] T. Belytschko, Y. Lu, L. Gu, Element-free Galerkin methods, International Journal for Numerical Methods in Engineering 34 (1994) 229–256.
[6] J. Dolbow, T. Belytschko, Volumetric locking in the element free Galerkin method, International Journal for Numerical Methods in Engineering 46 (1999) 925–942.
[7] K.J. Bathe, Finite Element Procedures, Prentice-Hall, Upper Saddle River, New Jersey, 1996.
[8] T.J. Hughes, The Finite Element Method. Linear Static and Dynamic Finite Element Analysis, Prentice-Hall, Inc., Englewood Cliffs, New Jersey, 1987, pp. 232–237.
[9] B.F. de Veubeke, Displacement and equilibrium models, in: O.C. Zienkiewicz, G. Hollister (Eds.), Stress Analysis, Wiley, London, 1965.
[10] J. Simo, M. Rifai, A class of mixed assumed strain methods and the method of incompatible modes, International Journal for Numerical Methods in Engineering 29 (1990) 1595–1638.
[11] J.C. Simo, F. Armero, R.L. Taylor, Improved versions of assumed enhanced strain tri-linear elements for 3D finite deformation problems, Computer Methods in Applied Mechanics and Engineering 110 (3–4) (1993) 359–386.
[12] P. Wriggers, S. Reese, A note on enhanced strain methods for large deformations, Computer Methods in Applied Mechanics and Engineering 135 (1996) 201–209.
[13] J. Simo, D. Fox, M. Rifai, On a stress resultant geometrically exact shell model. Part II: The linear theory; computational aspects, Computer Methods in Applied Mechanics and Engineering 73 (1) (1989) 53–92.
[14] N. Knight, Raasch challenge for shell elements, AIAA Journal 35 (2) (1997) 375–381.
[15] B.L. Kamp, C. Cho, S.W. Lee, A four-node solid-shell element formulation with assumed strain, International Journal for Numerical Methods in Engineering 43 (1998) 909–924.
[16] R.P. Cardoso, J.W. Yoon, R.A.F. Valente, A new approach to reduce membrane and transverse shear locking for one-point quadrature shell elements: linear formulation, International Journal for Numerical Methods in Engineering 66 (2) (2006) 214–249.
[17] S. Timoshenko, J.N. Goodier, Theory of Elasticicity, second ed., McGraw-Hill Book Company, Inc., 1951.